Mutant lamins cause mechanically-induced nuclear envelope rupture, DNA damage, and DNA-PK activation in muscle

Ashley J. Earle[1,*], Tyler J. Kirby[1,*], Gregory R. Fedorchak[1,*], Philipp Isermann[1], Jineet Patel[1], Sushruta Iruvanti[1], Gisèle Bonne[2], Lori L. Wallrath[3], Jan Lammerding[1,#]

[1] Meinig School of Biomedical Engineering & Weill Institute for Cell and Molecular Biology, Cornell University, Ithaca, NY, USA
[2] Sorbonne Université, Inserm UMRS 974, Center of Research in Myology, Association Institute of Myology, Paris, France
[3] Department of Biochemistry, University of Iowa, Iowa City, IA, USA
[*] These authors contributed equally
[#] Correspondence should be addressed to:
Jan Lammerding
Weill Hall, Room 235, Ithaca, NY 14853, USA
jan.lammerding@cornell.edu

ABSTRACT

Mutations in the human *LMNA* gene, which encodes the nuclear envelope proteins lamins A and C, cause Emery-Dreifuss muscular dystrophy (EDMD), congenital muscular dystrophy, limb-girdle muscular dystrophy, and a spectrum of other diseases. The molecular mechanisms responsible for these diseases remain incompletely understood, but the muscle-specific defects suggest that mutations may render nuclei more susceptible to mechanical stress. Using three mouse models of muscle laminopathies, we found that *Lmna* mutations reduced nuclear stability and caused widespread nuclear damage in skeletal muscle cells *in vitro* and *in vivo*, including the formation of chromatin protrusions, transient rupture of the nuclear envelope, DNA damage, and activation of DNA damage response pathways. Nuclear damage resulted from nuclear movement in maturing myotubes, and could be reversed by depletion of kinesin-1 or stabilization of microtubules surrounding the myonuclei. Inhibiting DNA-dependent protein kinase (DNA-PK), a major DNA damage response pathway, improved myofiber health, suggesting that DNA damage response signaling, rather than nuclear damage itself, causes the striated muscle defects. These findings point to the importance of DNA damage response pathways in post-mitotic muscle cells and open the door for novel therapeutic approaches for these currently untreatable diseases.

INTRODUCTION

The nuclear envelope proteins lamin A and C, together with the B-type lamins B1 and B2, are the major components of the nuclear lamina, which underlies the inner nuclear membrane. Lamins A/C play important roles in providing structural support to the nucleus and connecting the nucleus to the cytoskeleton[1]. In addition, they participate in transcriptional regulation, genome organization, and DNA damage and repair[1-4]. The majority of the over 450 *LMNA* mutations identified to date are responsible for autosomal dominant Emery-Dreifuss muscular dystrophy (EDMD)[5]. EDMD is characterized by slowly progressive skeletal muscle wasting, contractures of the elbow, neck, and Achilles tendons, a rigid spine, abnormal heart rhythms, heart block, and cardiomyopathy[6]. It remains unclear how *LMNA* mutations result in these tissue-specific defects, and the incomplete understanding of the disease pathogenesis presents a major hurdle in the development of effective treatment approaches. A major hypothesis regarding the disease mechanisms states that mutations in the *LMNA* gene result in mechanically weaker nuclei, making them more susceptible to force induced damage in mechanically stressed tissues, such as muscle, and leading to progressive muscle loss[4].

Previous studies have reported anecdotal evidence of severe ultrastructural nuclear damage—including blebbing and partial loss of the nuclear envelope, protrusion of chromatin into the cytoplasm, and intrusion of cytoplasmic organelles into the nucleoplasm—in skeletal muscle fibers of patients with EDMD[7-10], cardiac myocytes in *LMNA*-dilated cardiomyopathy patients[11, 12], lamin A/C-deficient mice[13, 14], and muscle and tendons of lamin-deficient fruit flies[15, 16]. However, systematic studies addressing the prevalence of these structural nuclear defects and the role of nuclear damage in the disease pathology remain elusive. Using three independent mouse models of striated muscle laminopathies, we evaluated the effect of *Lmna* mutations on nuclear mechanics and the downstream consequences in muscle cells *in vitro* and *in vivo*. We found that *Lmna* mutant muscle cells had structurally weaker nuclei, resulting in extensive nuclear damage *in vitro* and *in vivo*. The mechanically induced nuclear damage was associated with severe DNA damage in post-mitotic muscle cells. Intriguingly, the resulting activation of DNA damage response pathways, rather than the nuclear damage itself, was responsible for the progressive decline in myofiber health, suggesting that inhibition of DNA damage response pathways could serve as a novel therapeutic approach for laminopathies affecting striated muscle.

RESULTS

Lmna mutations cause progressive decline in myofiber health *in vitro* and *in vivo*

To examine the effect of *Lmna* mutations on nuclear mechanics and muscle function *in vitro*, we isolated myoblasts from three established mouse models of striated muscle laminopathies, representing a spectrum of disease severity: *Lmna*$^{-/-}$ mice[13], subsequently referred to as lamin A/C-knock-out mice (*Lmna* KO); knock-in mice carrying the *Lmna*$^{N195K/N195K}$ mutation (*Lmna* N195K)[17]; knock-in mice carrying the *Lmna*$^{H222P/H222P}$ mutation (*Lmna* H222P)[18]; and wild-type littermates (Fig. 1A). While the *Lmna* N195K mice were originally described as a model for dilated cardiomyopathy[17], in the C57BL/6 background used here, the mice developed pronounced muscular dystrophy in addition to the cardiac defects (Suppl. Fig. S1). For *in vitro* studies, we utilized a recently developed, three-dimensional culture protocol to differentiate primary

myoblasts into mature, contractile myofibers over the course of 10-14 days (Fig. 1B)[19]. The resulting myofibers display the highly organized sarcomeric structure and myonuclear positioning characteristic of mature skeletal muscle fibers *in vivo* (Suppl. Fig. S2).

All myoblasts, including the *Lmna* KO, *Lmna* N195K and *Lmna* H222P mutant cells, successfully completed myoblast fusion, differentiation into myotubes, formation of sarcomeric structures, and maturation into myofibers (Fig. 1C), consistent with previous studies on differentiation of *Lmna* KO and *Lmna* H222P myoblast into myotubes[20-22]. Wild-type myofibers remained healthy and highly contractile up to 14 days of differentiation, however, the *Lmna* mutant myofibers showed a decline in health, reduction in total cell area, and loss of contractility by ten days (Fig. 1C-E; Suppl. Fig. S3, Suppl. Movies 1-4). The reduction in total cell area at day 10 in the *Lmna* KO myofibers was associated with an increase in activated caspase-3 (Suppl. Fig. S4), indicating that at least some myofiber loss was due to cell-intrinsic apoptosis. Notably, the loss of muscle cell health, contraction, and total cell area closely correlated with the severity of the disease in the corresponding mouse models, with *Lmna* KO myofibers having the most severe phenotype, followed by the *Lmna* N195K and then the *Lmna* H222P models.

Lmna mutant muscle cells exhibit defective nuclear stability that correspond with disease severity

Previous studies found that lamin mutations linked to muscular disease reduced nuclear stability in patient-derived skin fibroblasts and in a Drosophila model[23]. To test whether reduced nuclear stability contributed to the progressive deterioration of *Lmna* mutant myofibers, we measured the nuclear deformability in primary myoblasts from the three laminopathy models using a novel microfluidics-based cell aspiration assay (Fig. 2A, Suppl. Movie 5). This assay is a higher throughput variation of the traditional micropipette aspiration technique commonly used to study nuclear mechanics[24, 25]. Nuclei from *Lmna* KO and *Lmna* N195K myoblasts were substantially more deformable than nuclei from wild-type controls (Fig. 2B, C). Intriguingly, myoblasts from *Lmna* H222P mice, which have a much later disease onset and less severe muscle defects than the other two *Lmna* mutant models (Fig. 1A), had only a modest increase in nuclear deformability relative to wild-type controls (Supp. Fig. S5A). Ectopic expression of lamin A significantly reduced the nuclear deformability defect in primary *Lmna* KO myoblasts (Suppl. Fig. S5B-D), confirming that the impaired nuclear stability was a direct consequence of altering the nuclear lamina. In addition, primary myoblasts from *Mdx* mice, which develop mild muscular dystrophy due to loss of dystrophin, a cell membrane protein, had nuclear deformation indistinguishable from wild-type controls (Suppl. Fig. S6), indicating that the defects in nuclear stability are specific to *Lmna* mutations and not muscular dystrophy in general.

To assess whether the observed defects in nuclear stability also occur in more mature, multinucleated myofibers, we subjected *Lmna* KO and wild-type myofibers to a 'microharpoon' assay[26, 27], in which precise strain is exerted on the perinuclear cytoskeleton, and the induced nuclear deformation and displacement are used to infer nuclear stability and nucleo-cytoskeletal coupling, respectively[26]. *Lmna* KO myofibers had significantly more deformable nuclei than wild-type controls (Fig. 2D, E; Suppl. Movie 6), consistent with the micropipette aspiration results in the myoblasts. Furthermore, analysis of *Lmna* mutant and wild-type myofibers at five days of *in vitro* differentiation revealed that *Lmna* KO, *Lmna* N195K, and *Lmna* H222P myofibers had significantly elongated myonuclei compared to wild-type controls (Fig. 2F, G), consistent with

decreased nuclear stability in the *Lmna* mutant cells and with previous reports of elongated nuclei in muscle biopsies from laminopathy patients[28]. Taken together, these findings suggest that myopathic *Lmna* mutations result in mechanically weaker myonuclei.

Lmna mutant myonuclei display nucleus-intrinsic chromatin protrusions

Analysis of nuclear shape and structure in myofibers differentiated from *Lmna* KO, *Lmna* N195K, and *Lmna* H222P myoblasts revealed striking chromatin protrusions that were completely absent in wild-type fibers. These protrusions extended beyond the (B-type) nuclear lamina up to tens of microns into the cytoplasm (Fig. 3A, B) and were enclosed by nuclear membranes, as indicated by the frequent presence of the nuclear membrane protein emerin, and occasionally nesprin-1 (Suppl. Fig. S7A); however, these proteins were often concentrated in punctae inside the protrusions and myonuclei. Other nuclear envelope proteins, such as nuclear pore complex proteins, were largely absent from the protrusions (Supp. Fig. S7B), suggesting an altered membrane composition in the chromatin protrusion, similar to what has been reported in analogous structures in cancer cells[29, 30].

The frequency of chromatin protrusion was highest in *Lmna* KO myofibers, followed by *Lmna* N195K and then *Lmna* H222P myofibers (Fig. 3B), correlating with the increased nuclear deformability *in vitro* (Fig. 2) and the disease severity *in vivo* (Fig. 1A). Intriguingly, while *Lmna* KO and *Lmna* N195K myofibers had extensive chromatin protrusions at five days of differentiation, the frequency of chromatin protrusions in the *Lmna* H222P cells was initially very low, but increased significantly from five to ten days of differentiation (Fig. 3B), matching the delayed disease onset and progressive phenotype *in vivo.* Ectopic expression of lamin A in *Lmna* KO myoblasts significantly reduced the occurrence of chromatin protrusions at ten days of differentiation (Fig. 3B), confirming that the protrusions were caused by loss of lamin expression.

Single muscle fibers isolated from the hindlimbs of *Lmna* mutant mice had similar chromatin protrusions (Fig. 3C, D), confirming their presence *in vivo*. In contrast, chromatin protrusions were not detectable in muscle fibers from wild-type mice (Fig. 3C, D). Interestingly, the prevalence of chromatin protrusions in the *Lmna* mutant myonuclei strongly depended on the location within the muscle. Myonuclei at the myotendinous junctions (MTJ) had significantly higher rates of chromatin protrusions than nuclei in the muscle fiber body (Fig. 3D).

To address whether the observed nuclear defects in *Lmna* mutant muscle cells are nucleus intrinsic, or arise from altered signaling pathways or other cytoplasmic changes in the mutant cells, we generated "hybrid" myofibers by combining *Lmna* KO and wild-type myoblasts. Following differentiation and myoblast fusion, these cells formed myofibers that contained both *Lmna* KO and wild-type nuclei with a shared cytoplasm (Fig. 3E). We quantified the number of nuclei with chromatin protrusions and compared genetically identical nuclei (e.g., wild-type or *Lmna* KO) from hybrid and isogenic control myofibers after 10 days of differentiation (Fig. 3F), with the genotype of each myonucleus determined by antibody staining against lamin A (Fig. 3E). Hybrid myofibers comprising ~80% wild-type nuclei and ~20% *Lmna* KO nuclei appeared healthy. Nonetheless, *Lmna* KO nuclei within the hybrid myofibers showed the same relative frequency of chromatin protrusions as nuclei from isogenic *Lmna* KO myofibers (Fig. 3F). Conversely, wild-type nuclei in hybrid fibers were not adversely affected by the presence of *Lmna* KO nuclei and lacked chromatin protrusions (Fig. 3F). These results indicate that the defects in nuclear structure

are intrinsic to the *Lmna* mutant myonuclei and not due to impaired muscle fiber health, altered cytoplasmic signaling, or changes in the cytoplasmic architecture in *Lmna* mutant muscle fibers.

Nuclei in lamin A/C-deficient myofibers experience extensive nuclear envelope rupture *in vitro* and *in vivo*

In addition to nuclear blebbing and protrusions of chromatin into the cytoplasm, muscle cells of patients with EDMD have anecdotally been found to contain inclusion of cytoplasmic organelles in the nucleoplasm[7-10], suggesting transient loss of nuclear envelope integrity. Furthermore, depletion of lamins, combined with cytoskeletal forces exerted on the nucleus, can result in nuclear envelope rupture[29, 31-35]. To examine whether the reduced nuclear stability seen in *Lmna* mutant muscle cells (Fig. 2) leads to nuclear envelope rupture in *Lmna* mutant myofibers, we genetically modified primary myoblasts to co-express a fluorescent nuclear envelope rupture reporter, consisting of a green fluorescent protein with a nuclear localization signal (NLS-GFP)[29] and fluorescently labeled histone (H2B-tdTomato). NLS-GFP is normally localized to the nucleus, but rapidly spills into the cytoplasm upon loss of nuclear membrane integrity and is then gradually reimported into the nucleus after the nuclear membrane has been repaired[29]. *In vitro* differentiated *Lmna* KO myotubes frequently exhibited nuclear envelope ruptures (Suppl. Movie 7), which were absent in wild-type controls. To investigate nuclear envelope rupture in more detail, we stably modified primary myoblasts with another fluorescent nuclear envelope rupture reporter, cGAS-mCherry. Upon nuclear envelope rupture, the cytoplasmic cGAS-mCherry reporter binds to the exposed genomic DNA and accumulates at the rupture site[29] (Fig. 4A); unlike the transient cytoplasmic NLS-GFP signal, however, the cGAS-mCherry accumulation persists even after the nuclear envelope has been repaired[29, 31]. *Lmna* KO myotubes displayed a progressive increase in the number of nuclear cGAS-mCherry foci during differentiation, starting around day two, which could be rescued by ectopic expression of wild-type lamin A (Fig. 4A, B). Accumulation of cGAS-mCherry in wild-type myotubes was hardly detectable (Fig. 4B). *Lmna* N195K showed intermediate levels of nuclear envelope rupture (Suppl. Fig. S8), whereas *Lmna* H222P myotubes had cGAS-mCherry accumulation comparable to wild-type controls, consistent with the milder defects in nuclear stability in the *Lmna* H222P mutant cells (Suppl. Fig. S8).

To test whether nuclear envelope rupture occurs within *Lmna* KO muscle *in vivo*, we generated transgenic mice that express a fluorescent cGAS-tdTomato nuclear rupture reporter and crossed these mice into the *Lmna KO* mouse model. Single hindlimb muscle fibers isolated from *Lmna* KO offspring expressing the cGAS-tdTomato reporter revealed a large fraction of myonuclei with cGAS-tdTomato foci, which were absent in wild-type littermates expressing the cGAS-tdTomato reporter and in *Lmna* KO mice not expressing the cGAS-tdTomato reporter (Fig. 4C, D). Within *Lmna* KO muscle fibers, the frequency of nuclear envelope rupture was significantly higher at the MTJ than in the myofiber body nuclei (Fig. 4D; Suppl. Fig. S9), consistent with the increased frequency of chromatin protrusions in the MTJ myonuclei. As an independent approach to detect loss of nuclear-cytoplasmic compartmentalization in muscle fibers, we analyzed the intracellular localization of endogenous heat shock protein 90 (Hsp90), which is typically excluded from the nucleus[36]. Muscle fibers isolated from *Lmna* KO mice, but not wild-type littermates, had a significant increase in nuclear Hsp90 (Suppl. Fig. S10), confirming the occurrence of nuclear envelope rupture *in vivo*. In our *in vitro* assays, all three *Lmna* mutant models revealed increased nuclear Hsp90 levels during myoblast differentiation (Suppl. Fig. S10). Taken together, these findings indicate widespread nuclear envelope rupture in laminopathic skeletal muscle.

Nuclear damage in *Lmna* KO myofibers can be prevented by microtubule stabilization

We surmised that nuclear envelope ruptures in *Lmna* mutant myofibers resulted from cytoskeletal forces acting on mechanically weak myonuclei, and that reducing mechanical stress on the nuclei would decrease nuclear damage. In striated muscle cells, microtubules form a cage-like structure around the myonuclei[37] (Suppl. Fig. S11). To test if stabilizing this microtubule network and thereby reinforcing myonuclei can reduce chromatin protrusions and nuclear envelope rupture, we treated *in vitro* differentiated myoblasts with low doses of the microtubule stabilizing drug, paclitaxel. Here and in the following work, we focused on the *Lmna* KO model, which showed the most severe nuclear defects. The microharpoon assay confirmed that microtubule stabilization reinforced *Lmna* KO nuclei in differentiated myofibers and significantly reduced nuclear deformation in response to cytoplasmic force application (Fig. 4E, Suppl. Movie 8). Furthermore, paclitaxel treatment significantly reduced the percentage of nuclei with chromatin protrusions (Fig. 4F) and the incidence of nuclear envelope rupture detected with the cGAS-mCherry reporter in the *Lmna* KO cells (Fig. 4G), suggesting that nuclear damage indeed arises from mechanical stress on the myonuclei.

Lmna* KO myonuclei have increased levels of DNA damage *in vitro* and *in vivo

Recent studies found that nuclear deformation and nuclear envelope rupture can cause DNA damage in migrating cells[29, 31, 38]. To investigate whether chromatin protrusions and nuclear envelope rupture can similarly lead to DNA damage in muscle cells, we quantified DNA damage in differentiating primary myoblasts by staining for γH2AX, a marker for double stranded DNA damage[39]. Both *Lmna* KO and wild-type myoblasts had elevated levels of DNA damage at the onset of differentiation (Fig. 5A, B), consistent with previous reports that show the transition from myoblasts to myotubes is associated with a transient increase in γH2AX levels[40, 41]. However, while γH2AX levels in wild-type myotubes subsequently decreased and then remained stable at low levels, the fraction of myonuclei with severe DNA damage in the *Lmna* KO cells continued to increase from day five to ten days post differentiation, with nearly 20% of *Lmna* KO myonuclei exhibiting severe DNA damage by day 10 (Fig. 5B). Single muscle fibers isolated from *Lmna* KO mice similarly contained many myonuclei with severe γH2AX staining (Fig. 5C, D), confirming the presence of extensive DNA damage in *Lmna* KO muscle fibers *in vivo*. In contrast, muscle fibers isolated from wild-type mice contained only low levels of DNA damage (Fig. 5C, D).

Kinesin-mediated nuclear migration is responsible for nuclear damage in *Lmna* KO myonuclei

Because the levels of nuclear damage and DNA damage were intrinsic to individual nuclei, we surmised that these defects arose from cytoskeletal forces acting on mechanically weaker nuclei. These forces could be generated by contractile actomyosin machinery that becomes increasingly organized during muscle differentiation, or from microtubule-associated motors involved in positioning myonuclei during early myotube maturation[42, 43]. Treatment of *Lmna* KO and wild-type myotubes with nifedipine, a calcium channel blocker, effectively abrogated myotube contraction, but did not reduce the frequency of chromatin protrusions in *Lmna* KO myonuclei (Suppl. Fig. S12). Therefore, we focused our attention to cytoskeletal forces exerted on the nucleus during nuclear migration in differentiating myotubes.

Time-lapse sequences of *Lmna* KO myoblasts expressing the NLS-GFP and/or cGAS-mCherry reporters revealed that nuclear envelope rupture frequently occurred during early stages of myotubes maturation, when the initially clustered nuclei are distributed along the length of myotubes by microtubule-associated motors (Fig. 6A). Furthermore, chromatin protrusion lengths continued to increase during maturation in *Lmna* mutant myotubes (Suppl. Fig. S13). If chromatin protrusions and nuclear envelope rupture are caused by nuclear migration, then abolishing nuclear movement should reduce or prevent nuclear defects. Affirming this hypothesis, depletion of Kif5b, a subunit of kinesin-1 that is necessary for nuclear migration[42-44], almost completely abolished chromatin protrusions (Fig. 6B, C; Suppl. Fig. S14) and nuclear envelope rupture (Fig. 6D, E) in *Lmna* KO myotubes. Furthermore, Kif5b depletion also substantially reduced DNA damage in the *Lmna* KO myotubes (Fig. 6F, G), lending further support to the idea that DNA damage is linked to nuclear envelope rupture.

Decline of *Lmna* KO myofiber health is linked to activation of DNA-PK DNA damage response pathway

While our studies linked muscle dysfunction to DNA damage, it was unclear if the DNA damage itself was causal for the defective muscle phentypes. Prior studies showed that increased activity of DNA-dependent protein kinase (DNA-PK), one of the major DNA damage sensing pathways[45], is linked to the age-related decline of metabolic, mitochondrial and physical fitness of skeletal muscle cells[36]. In our experiments, DNA-PK activity significantly increased in *Lmna* KO myotubes during differentiation (Fig. 7A), matching the progressive increase in DNA damage (Fig. 5B).

To test whether increased DNA-PK activity was functionally involved in *Lmna* KO myofiber decline, we treated developing *Lmna* KO myofibers with the DNA-PK-specific inhibitor NU7441. Intriguingly, despite the continued presence of chromatin protrusions and nuclear envelope rupture, DNA-PK inhibition significantly improved the viability and health of *Lmna* KO myofibers (Fig. 7B, C; Suppl. Movies 9, 10). Independent inhibition of ATM and ATR, the other major cellular DNA damage response pathways[45], did not significantly improve myofiber health (Suppl. Fig. S15). Taken together, these findings indicate that the mechanically induced DNA damage and the resulting DNA-PK activation are responsible for the progressive myofiber decline in laminopathies.

DISCUSSION

Here, we present comprehensive evidence from multiple *in vitro* and *in vivo* models of striated muscle laminopathies that demonstrate that *Lmna* mutations result in mechanically weaker myonuclei that experience substantial nuclear damage in muscle cells and tissues including chromatin protrusions, transient nuclear envelope rupture, and increased DNA damage. Intriguingly, the nuclear damage did not arise from muscle contractions, but from kinesin-1 mediated forces during nuclear migration, a key element in muscle differentiation and maturation[43]. Furthermore, we found that the DNA-PK activation in response to the mechanically induced DNA damage, rather than the nuclear damage itself, was driving the progressive decline in myofiber health in the *Lmna* mutant cells. This result was surprising, as DNA-PK inhibition significantly improved myofiber health despite the continued presence of chromatin protrusions

and nuclear envelope rupture. Taken together, our findings support a model in which cytoskeletal forces cause chromatin protrusions and nuclear envelope ruptures in mechanically weakened muscle cell nuclei, triggering DNA damage and activation of the DNA-PK pathway, which then leads to myofiber dysfunction and death (Fig. 8).

While we cannot exclude the possibility that altered cytoplasmic signaling pathways and impaired DNA damage repair in *Lmna* mutant myocytes contribute to the increased DNA damage[46], the finding that Kif5b depletion significantly reduced DNA damage in *Lmna* KO cells suggest that the observed DNA damage was mechanically induced. Nonetheless, it remains unclear how nuclear damage and nuclear envelope rupture cause DNA damage. Possible mechanisms include exposure of genomic DNA to cytoplasmic nucleases or nuclear exclusion and efflux of DNA repair, as previously discussed in the context of confined cell migration[47, 48].

Although we have seen abundant evidence of progressive cell death associated with nuclear envelope rupture and severe DNA damage, further investigations into the precise cause of myofiber decline and death are warranted. Muscle tissue is generally considered resistant to apoptosis and non-necrotic types of death have not been completely characterized[49]. In our studies, we found evidence of caspase-3 activation, but additional mechanisms, possibly triggered by DNA-PK activation, may further contribute to the decline in myocyte health, consistent with the recently identified role of DNA-PK in age-associated decline in muscle function[36] or canonical DNA-PK signaling[39]. DNA-PK signaling has been implicated in accelerated aging through telomere shortening, AMPK inhibition, fatty acid synthesis, and mitochondrial loss, with effects mediated by the phosphorylation of HSP90α in muscle cells[36, 50]. Interestingly, DNA-PK phosphorylates a number of other heat shock proteins, including HSP70 and HSP150, as well as lamin B1, β-tubulin, desmoplakin and vimentins[51], which could further contribute to disease progression in skeletal muscle of laminopathies.

In the *in vitro* models, kinesin-1 mediated nuclear movement was the main driver of nuclear damage. *In vivo*, however, acto-myosin generated forces are likely substantially larger than in the *in vitro* differentiated myofibers, and may further contribute to nuclear damage, particularly in mature muscle fibers. At the same time, the ongoing regeneration in dystrophic muscle[52] may result in an increased frequency of nuclear movement even in adult animals, which could further exacerbate the disease development. Insufficient anchoring of myonuclei within the muscle fiber, for example, at neuromuscular junctions[53], could further promote nuclear damage *in vivo*. Contraction-induced nuclear damage may be particularly relevant in cardiac myocytes, whose dysfunction are the primary cause of death in striated muscle laminopathies[2]. Interestingly, our *in vivo* studies found that nuclear envelope rupture and DNA damage were more prevalent at the MTJ compared to the muscle body. The increased damage at the MTJ may be due to locally higher forces, altered nucleo-cytoskeletal organization, or yet to be identified factors. Intriguingly, the MTJ enriched nuclear damage correlates with previous findings of increased nuclear abnormalities and altered transcription at the MTJ in *Lmna* KO mice[54] and the clinical progression of EDMD in humans, which starts with joint contractures before the onset of muscle atrophy[6, 55, 56].

Overall, these findings demonstrate the importance of lamins A/C to provide structural support to myonuclei required for healthy muscle function, and indicate that mechanically induced DNA damage and DNA-PK activation cause cellular decline and death even in postmitotic cells.

Importantly, the work presented here point to potential new clinical avenues for the currently untreatable laminopathies. While stabilizing microtubules with low doses of paclitaxel and depletion of kinesin-1 both reduced damage in *Lmna* KO myofibers, the associated detrimental long-term effects may preclude therapeutic use. In contrast, DNA-PK inhibition significantly improved myofiber health without adverse effects *in vitro*, even at 14 days (Fig. 7), and has already been used in anti-cancer therapy in patients[57]. Thus, the striking effects of DNA-PK inhibition on *Lmna* KO myofiber health raises the exciting prospect of novel therapeutic approaches for laminopathies affecting striated muscle function.

Lastly, beyond striated muscle laminopathies, insights gained from this work are highly relevant to other biological systems in which nuclei are exposed to physical stress from the cytoskeleton. Examples include confined migration[58] or intracellular nuclear positioning in muscle, polarized epithelial, or neuronal cells[59]. In the brain, kinesin-1 applies localized forces to the nuclei of migrating neurons during cortex formation[60]. Since cortical neurons lack lamin A[61], thus leaving B-type lamins as the major nuclear lamina components in these cells, nuclear damage through kinesin-mediated forces may lead to the severe neurodevelopment defects and nuclear abnormalities during brain development in mice lacking B-type lamins[62]. Taken together, these findings point to an important role of mechanically induced nuclear damage and activation of DNA damage response pathways, which could open new areas of research, particularly in post-mitotic cells, where DNA damage response pathways are currently underexplored.

METHODS

Animals. *Lmna* KO (*Lmna*$^{-/-}$)[13], *Lmna* H222P (*Lmna*$^{H222P/H222P}$)[18], and *Lmna* N195K (*Lmna*$^{N195K/N195K}$)[17] have been described previously. *Lmna*$^{+/-}$, *Lmna*$^{H222P/+}$, and *Lmna*$^{N195K/+}$ mice were backcrossed at least seven generations into a C57-BL/6 line. For each mouse model, heterozygous mice were crossed to obtain homozygous mutants, heterozygous mice, and wild-type littermates. *Lmna* mutant mice were provided with gel diet (Nutri-Gel Diet, BioServe) supplement to improve hydration and metabolism upon onset of phenotypic decline. *Dmd*^{mdx} mice have been described previously[63]; mice were obtained from the Jackson Laboratory in a C57BL background and hemi- or homozygous animals were bred to produce all hemi- and homozygous offspring. All mice were bred and maintained according to IACUC approved protocols. Data from wild-type littermate controls for *Lmna* KO, *Lmna* N195K and *Lmna* H222P showed no difference in any of the experimental outcomes between the different wild-type littermates, so wild-type data was combined into a single group unless otherwise specified. For both *in vivo* and *in vitro* studies, cells and or tissues were isolated from a single mouse and counted as a single replicate. All data are based on at least two independently derived primary cell lines for each genotype.

Nuclear envelope rupture reporter mouse (cGAS/MB21D1-tdTom transgenic mouse). To detect NE ruptures *in vivo,* we generated a transgenic mouse expressing FLAG tagged human cGAS$^{E225A/D227A}$ fused to a tdTomato fluorescent protein (cGAS-tdTomato) under the control of the commonly used constitutive active CMV promoter. The cGAS mutations are in the magnesium-binding domain, abolishing the enzymatic activity and downstream production of interferon, while still remaining the ability to bind to genomic DNA. The mammalian expression cassette including promoter and terminator (CMV-3xFLAG-cGAS$^{E225A/D227A}$-tdTomato-SV40polyA) was released from the expression vector, removing the prokaryotic domains. The purified linear DNA was then injected into the pronucleus of fertilized embryos collected from super-ovulated C57BL/6 mice and transplanted into pseudo-pregnant recipients. The resulting transgenic mouse model was used to cross into the *Lmna* KO background to generate 3×FLAG-cGAS$^{E225A/D227A}$-tdTomato positive *Lmna* KO mice within two generations.

Myoblast isolation. Cells were harvested from *Lmna* KO, *Lmna* N195K, *Lmna* H222P, and wild-type littermates between 3-5 weeks for *Lmna* KO mice, 4-6 weeks for *Lmna* N195K, and 4-10 weeks for *Lmna* H222P mice using a protocol adapted from[13]. With the exception of the *Lmna* KO myoblasts, these time-points were prior to the onset of disease phenotypes. Myoblasts from wild-type littermates were harvested at the same time. Muscles of the lower hindlimb were isolated, cleaned of fat, nerve and excess fascia, and kept in HBSS on ice until all mice were harvested. The muscles were digested in 4 ml:1 g of tissue wet weight in a solution of 0.5% Collagenase II (Worthington Biochemicals), 1.2 U/ml Dispase (Worthington Biochemicals), 1.25 mM $CaCl_2$ (Sigma) in HBSS/25 mM HEPES buffer. Digestion was carried out in a 37˚C water bath for a total time of 60 minutes. At 20 minutes intervals, digestion cocktails were removed and triturated 40 times with a 5 ml pipet. In the case of difficult to digest tissues, an extra 25% of 1% Collagenase II was added to the digestion after 40 minutes.

When tissues were fully digested, the reaction was quenched using equal volumes of DMEM supplemented with 10% fetal bovine serum (FBS) and 1% P/S (D10 media, Gibco). The cell suspension was strained through 40 and 70 µm filters (Greiner Bioscience) sequentially to remove

undigested myotube fragments and tendon. The cell suspension was centrifuged at 800 × g for 5 minutes and washed with 8 ml of D10 media for a total of four times. Cells were then resuspended in primary myoblast growth media (PMGM; Hams F-10 (Gibco) supplemented with 20% horse serum and 1% penicillin/streptomycin and 1 µl/ml basic fibroblast growth factor (GoldBio)) and plated onto a 2 % gelatin coated T25 flask. Cells were allowed to sit undisturbed for 72 hours. Capitalizing on the fact that myoblasts adhere much more weakly than fibroblasts, cells were passaged using PBS (calcium- and magnesium-free) instead of trypsin to purify the myoblasts. Cells were washed for 2-3 minutes at room temperature using a volume of PBS sufficient to coat the bottom of the flask and dislodged using manual agitation. When necessary, a 0.000625% trypsin solution was used to aid in the myoblast removal. Myoblasts were re-suspended in PMGM and re-plated onto gelatin coated flasks. This process was continued 3-4 times until pure myoblast cultures were achieved[64]. Cells were maintained in culture on gelatin coated flasks with media changes every other day. All experiments were carried out prior to passage 12. Each independent experiment was done on a different set of lamin mutant and wild-type littermates such that each independent experiment was sourced from a different animal to account for heterogeneity in phenotype.

Myoblast differentiation. Myoblasts were differentiated according to a protocol modified from [19]. Coverslips for differentiation were prepared by first coating with CellTak (Corning) according to the manufacturer's protocol and then coating with growth factor reduced Matrigel (Corning) diluted 1:100 with IMDM with Glutamax (Gibco). Pre-cooled pipette tips were used to avoid premature polymerization. Matrigel was allowed to polymerize at 37˚C for 1 hour and the excess solution was aspirated. Primary myoblasts were seeded at a density of 55,000 cells/cm^2 in PMGM. Cells were allowed to attach for 24 hours before being switched to primary myoblast differentiation media (PMDM) composed of IMDM with Glutamax and 2% horse serum. One day after the onset of differentiation, a top coat of 1:3 Matrigel:IMDM was added to the cells and allowed to incubate for 1 hour at 37˚C. PMDM supplemented with 100 ng/ml agrin (R&D Systems) was added to the cells and henceforth replaced every second day. Cells were allowed to differentiate for a total of 0, 5, or 10 days.

Plasmids and generation of fluorescently labeled cell lines. Each of the mutant myoblast lines were stably modified with lentiviral vectors to express the nuclear rupture reporter NLS-GFP (pCDH-CMV-NLS-copGFP-EF1-blastiS) and cGAS-mCherry (pCDH-CMV-cGAS$^{E225A/D227A}$-mCherry2-EF1-blastiS. cGAS is a cytosolic DNA binding protein; we used a cGAS mutant (E225A/D227A) with abolished enzyme activity and interferon production, but that still binds DNA[65] and serve as a nuclear envelope rupture reporter[29]. For rescue experiments, *Lmna* KO cells were modified with human lamin A (pCDH-CMV-preLamin A-IRES-GFP-puro).

Viral modification. Pseudoviral particles were produced as described previously[29]. In brief, 293-TN cells (System Biosciences, SBI) were co-transfected with the lentiviral plasmid using PureFection (SBI), following manufactures protocol. Lentivirus-containing supernatants were collected at 48 hours and 72 hours after transfection, and filtered through a 0.45 µm filter. Cells were seeded into 6-well plates so that they reached 50-60% confluency on the day of infection and transduced at most 2 consecutive days with the viral stock using the TransDux Max system (SBI). The viral solution was replaced with fresh culture medium, and cells were cultured for 24 hours before selection with 1 µg/mL of puromycin or 2 µg/mL blasticidin S for 2-5 days. After selection,

cells were subcultured and maintained in their recommended medium without the continued use of selection agents.

Extended imaging using incubator microscope. Long term imaging was performed using an Incucyte imaging system, which allows for incubator imaging to minimize the effects of humidity and CO_2 changes. The differentiating cells expressing combinations of NLS-GFP and cGAS-mCherry were imaged using the Incucyte dual color filter module from day 0 to day 10, every 30-60 minutes with a 20× objective. Resulting images were analyzed using the Incucyte software, which performs fluorescence background subtraction using a top hat method and then subsequent thresholding. cGAS-mCherry cells were thresholded and then analyzed for increase in fluorescent foci over time to track the rate of increase in nuclear envelope rupture or damage. NLS-GFP cells were used to investigate the frequency and presence of nuclear envelope rupture. To verify the results obtained from the Incucyte, cells were fixed and stained with appropriate antibodies to evaluate DNA damage and nuclear envelope rupture.

Isolation of single muscle fibers. Single muscle fibers were harvested in a protocol adapted from Vogler et al.[66]. As previously described, fibers were isolated from male and female *Lmna* KO and wild-type litter mates at 5-6 weeks of age and *Lmna* H222P and wild-type litter mates were harvested at 6-8 weeks of age at 23-25 weeks of age in order to compare pre- and post-phenotype onset tissue[13, 18, 67]. While *Lmna* H222P male and female mice show differences in cardiac defects, they do not exhibit differences in progression of skeletal muscle defects[18, 67], so both male and female mice were used for this analysis. Briefly, the EDL (extensor digitorus longus) and plantaris were isolated from the mouse and placed directly into a 1 ml solution of F10 media with 4,000 U/ml of Collagenase I (Worthington Biochemicals). The tissue was digested for 15-40 minutes depending on muscle size in a 37˚C water bath with agitation by inversion every 10 minutes. The reaction was quenched by transferring the digestion mixture to 4 ml of PMGM. Single fibers were hand-picked from the digested tissue using fire polished glass Pasteur pipettes. When necessary, the tissue was further dissociated by manual pipetting with a glass pipet. Fibers were washed once in fresh media prior to fixation with 4% paraformaldehyde (PFA) for 15 minutes at room temperature and subsequent IF staining.

Pharmacological treatments. For preliminary experiments, myoblasts were differentiated using the standard protocol and treated with pharmacological treatments starting at day 5 of differentiation. For chromatin protrusion studies, paclitaxel was administered to differentiated myotubes in two 24 hours bursts at day 4 and day 6-post differentiation with a 24 hour recovery in between. Myotubes were then fixed in 4% PFA at day 7 and stained with anti-lamin B and DAPI in order to quantify the percentage of myonuclei with chromatin protrusions. For long term studies using the cGAS reporter, myotubes were treated with 10 nM of paclitaxel starting at day 5 and then media was refreshed every day. To inhibit myotube contraction, cells were treated with 5 μM nifedipine starting at day 5 and then media was refreshed every day. For DNA damage inhibitor experiments, cells were treated with NU7441 (1 μM), KU55933 (5 μM) and VE-821 (5 μM) starting at day 7 of differentiation through day 14 of differentiation.

Biophysical assays. To evaluate nuclear deformability in high throughput, we designed and fabricated a microfluidic, micropipette aspiration device. The mask and wafers were produced in the Cornell NanoScale Science and Technology Facility (CNF) using standard lithography

techniques. PDMS molds of the devices were cast using Sylgard 184 (Dow Corning) and mounted on coverslips using a plasma cleaner as described previously[29]. Three port entrances were made using a 1.2 mm biopsy punch. Pressures at the inlet and outlet ports were set to 1.0 and 0.2 psi (relative to atmospheric pressure, P_{atm}), respectively, using compressed air regulated by a MCFS-EZ pressure controller (Fluigent) to drive single cells through the device. Myoblasts (~5×10^6 cells/mL suspended in 2 % bovine serum albumin (BSA), 0.2 % FBS and 10 µg/mL Hoechst 33342 DNA stain in PBS) were captured within an array of 18 pockets, and then forced to deform into 3 µm wide × 5 µm tall micropipettes. The selected pressures resulted in detectable nuclear deformations without causing significant damage to the cells (tested using propidium iodide staining). The remaining port was set to P_{atm} and outfitted with a handheld pipette to flush cells from the pockets at the start of each image acquisition sequence. Brightfield and fluorescence images were acquired every 5 seconds for a minimum of 60 seconds using an inverted microscope and 20×/NA 0.8 air objective. Nuclear protrusion length was calculated using a custom-written MATLAB program.

For the microharpoon studies, myoblasts were seeded in 35 mm glass bottom dishes and differentiated as previously described, except without the addition of a Matrigel top coat to allow microharpoon access. A Sutter P-97 micropipette puller was used to create microharpoons from borosilicate glass rods (Sutter; OD: 1.0 mm, ID: 0.78, 10 cm length) with tip diameters of ≈1 µm. Day 4 myotubes (*Lmna* KO and wild type) were treated for 24 hours with either 50 nM Paclitaxel or the corresponding 0.1% DMSO. The following day, the microharpoon assay was performed as previously described by our laboratory[26], with slight modifications to the pull parameters to accommodate myotubes. The microharpoon was inserted ≈5─7 µm from the edge of the nucleus and pulled 15 µm at a rate of 1 µm/s. Pull direction was always orthogonal to the long axis of the myofiber. Images were acquired at 40× (+1.6×) every 5 seconds. Nuclear strain and centroid displacement were calculated using a custom-written MATLAB program, made available upon request.

siRNA treatment. siRNAs used were as follows: Kif5b#3 (target sequence 5′-CAGCAAGAAGTAGACCGGATA-3′; Qiagen SI00176050), Kif5b#4 (target sequence 5′-CACGAGCTCACGGTTATGCAA-3′; Qiagen SI00176057), and non-target (NT) negative control (ON-TARGETplus non-targeting pool, Dharmachon, D-001810-10). Myoblasts were seeded on a Matrigel coating at a density of ~15,000 cells/well. Once adhered, the myoblasts were transfected twice, 48 hours apart, with siRNA for NT or Kif5b using Lipofectamine RNAiMAX at a concentration of 150 nM in PMGM. After 12 hours, the myoblasts were switched to PMDM and differentiated for 5 days.

Immunofluorescence staining. Cells were fixed in pre-warmed 4% PFA at the appropriate time point(s) and washed with PBS. Cells were blocked and permeabilized with a solution of 3% BSA, 0.1% Triton-X 100 and 0.1% Tween (Sigma) for 1 hour at room temperature. Cells were stained with primary antibodies diluted in blocking solution according to Table 2 at 4˚C overnight. Samples were washed with PBS and incubated for 1 hour at room temperature with 1:250 dilution of AlexaFluor antibodies (Invitrogen) and 1:1000 DAPI (Sigma). Single muscle fibers were stained using the same procedure in Eppendorf tube baskets with an increase in blocking solution Triton-X concentration to 0.25%.

Western blotting. Cells were lysed in RIPA buffer containing protease (cOmplete EDTA-Free, Roche) and phosphatase (PhosSTOP, Roche) inhibitors. Protein was quantified using Bio-Rad Protein Assay Dye and 25-30 µg of protein lysate was separated using a 4-12% Bis-Tris polyacrylamide gel using standard a standard SDS-Page protocol. Protein was transferred to a polyvinylidene fluoride (PVDF) membrane overnight at 4˚C at a current of 40 mA. Membranes were blocked using 3% BSA in tris-buffered saline containing 0.1% Tween-20 and primary antibodies (Table 2) were diluted in the same blocking solution and incubated overnight at 4˚C. Protein bands were detected using either IRDye 680LT or IRDye 800CW (LI-COR) secondary antibodies, imaged on an Odyssey® CLx imaging system (LI-COR) and analyzed in Image Studio Lite (LI-COR)

Imaging acquisition. Cells on coverslips and mounted single muscle fibers were imaged with an inverted Zeiss LSM700 confocal microscope. Z-stack were collected using 20× air (NA = 0.8), 40× water-immersion (NA = 1.2) and 63× oil-immersion (NA = 1.4) objectives. Airy units for all images were set between 1 and 1.5. Epi-fluorescence images were collected on a motorized inverted Zeiss Observer Z1 microscope equipped with CCD cameras (Photometrics CoolSNAP EZ or Photometrics CoolSNAP KINO) or a sCMOS camera (Hamamatsu Flash 4.0). H&E histology images were collected on an inverted Zeiss Observer Z1 microscope equipped with a color CCD camera (Edmund Optics, EO-0312C).

Image analysis. Image sequences were analyzed using ZEN (Zeiss), ImageJ, or MATLAB (Mathworks) using only linear adjustments uniformly applied to the entire image region. Region of interest intensities were extracted using ZEN or ImageJ. To quantify cell area and myofiber health, maximum intensity protections were generated, which were then blinded to the observer. Cell area was calculated using thresholding of the actin and myosin heavy chain fluorescent signal. Myofiber health was scored according to the scale provided in (Suppl. Fig. S3). To count the number of DNA protrusions, and DNA damage foci, confocal image stacks were three-dimensionally reconstructed and displayed as maximum intensity projections. Protrusions lengths were both counted and measured by the presence of DAPI signal beyond the lamin B rim of the nucleus. Aspect ratio was quantified based on a thresholded lamin B rim to avoid the confounding factor of the DNA protrusions outside the body of the nucleus. Nuclear rupture was detected by an increase of the cytoplasmic NLS-GFP signal, or the localization of cGAS-mCherry to the nucleus. For better visualization of NLS-GFP cells many of the fluorescent single color image sequences were inverted. Graphs were generated in Excel (Microsoft), and figures were assembled in Illustrator (Adobe). DNA damage was determined by counting H2AX foci and then binned based on foci number. If damage was so severe that individual foci could not be counted, these nuclei were placed in the >25 foci category. For Hsp90 quantification, average nuclear Hsp90 fluorescence intensity was determined from a single mid-nucleus z-plane image and normalized to the cytoplasmic intensity at two points immediately adjacent to the nucleus.

Statistical Analysis. Unless otherwise noted, all experimental results were taken from at least three independent experiments and *in vivo* data were taken from at least three animals. For data with normal distribution, we used either student's t-tests (comparing two groups) or one-way ANOVA (for experiments with more than two groups) with post-hoc tests. When multiple comparisons were made, we adjusted the significance level using Bonferroni corrections. All tests were performed using GraphPad Prism. Micropipette aspiration data were natural log-transformed (Suppl. Fig.

S5A) and analyzed by linear regression of the log-log data. In addition, data was analyzed with a multilevel model, in which the log-transformed protrusion length was the dependent variable in the model and the log-transformed time, genotype, and their interaction were treated as independent fixed effects. Variance from individual experiments and other effects were considered in the model as random effects. Post-hoc multiple comparisons test with Dunnett correction were performed to determine differences between *Lmna* mutant cells (*Lmna* KO, *Lmna* N195K, and *Lmna* H222P) and control cells (pooled wild-type). Analyses were carried out using JMP software. Unless otherwise noted, * denotes $p \leq 0.05$, ** denotes $p \leq 0.01$, and *** denotes $p \leq 0.001$. Unless otherwise indicated, error bars represent the standard error of the mean (SEM).

ACKNOWLEDGEMENTS

The authors thank Dr. Colin Stewart for providing the *Lmna* KO and *Lmna* N195K mouse models, Edgar Gomes for help with the *in vitro* myocyte differentiation protocol, Ryan Lin for scoring of myofiber health, Ishi Aron for quantification of cell area, Alexandra Corbin for *in vivo* and *in vitro* protrusion analysis and *in vivo* Hsp90 localization analysis, Rebecca Mount for optimization of single fiber isolation and subsequent analysis, Daniel Huang for quantification of the *Lmna* N195K skeletal muscle fiber cross-sectional areas, Francoise Vermeylen, Stephen Parry and Lynn Johnson from the Cornell Statistical Consulting Unit, and Katherine Strednak and the Cornell Center for Animal Resources and Education (CARE) for help in maintaining the *Lmna* mutant mice. This work was supported by awards from the National Institutes of Health [R01 HL082792 and U54 CA210184], the Department of Defense Breast Cancer Research Program [Breakthrough Award BC150580], and the National Science Foundation [CAREER Award CBET-1254846 and MCB-1715606], as well as generous gifts from the Mills family, a Fleming Postdoctoral Fellowship to T.K, and National Science Foundation Graduate Research Fellowships to A.E. [2013160437] and G.F. [2014163403]. This work was performed in part at the Cornell NanoScale Facility, a member of the National Nanotechnology Infrastructure Network, which is supported by the National Science Foundation [Grant ECCS-0335765].

REFERENCES

1. de Leeuw, R., Gruenbaum, Y. & Medalia, O. Nuclear Lamins: Thin Filaments with Major Functions. *Trends Cell Biol* **28**, 34-45 (2018).
2. Worman, H.J. Cell signaling abnormalities in cardiomyopathy caused by lamin A/C gene mutations. *Biochem Soc Trans* **46**, 37-42 (2018).
3. Naetar, N., Ferraioli, S. & Foisner, R. Lamins in the nuclear interior - life outside the lamina. *J Cell Sci* **130**, 2087-2096 (2017).
4. Davidson, P.M. & Lammerding, J. Broken nuclei--lamins, nuclear mechanics, and disease. *Trends Cell Biol* **24**, 247-256 (2014).
5. Maggi, L., Carboni, N. & Bernasconi, P. Skeletal Muscle Laminopathies: A Review of Clinical and Molecular Features. *Cells* **5** (2016).
6. Bechert, K., Lagos-Quintana, M., Harborth, J., Weber, K. & Osborn, M. Effects of expressing lamin A mutant protein causing Emery-Dreifuss muscular dystrophy and familial partial lipodystrophy in HeLa cells. *Exp Cell Res* **286**, 75-86 (2003).
7. Vigouroux, C. *et al.* Nuclear envelope disorganization in fibroblasts from lipodystrophic patients with heterozygous R482Q/W mutations in the lamin A/C gene. *J Cell Sci* **114**, 4459-4468 (2001).
8. Fidzianska, A. & Hausmanowa-Petrusewicz, I. Architectural abnormalities in muscle nuclei. Ultrastructural differences between X-linked and autosomal dominant forms of EDMD. *J Neurol Sci* **210**, 47-51 (2003).
9. Fidzianska, A., Toniolo, D. & Hausmanowa-Petrusewicz, I. Ultrastructural abnormality of sarcolemmal nuclei in Emery-Dreifuss muscular dystrophy (EDMD). *J Neurol Sci* **159**, 88-93 (1998).
10. Park, Y.E. *et al.* Nuclear changes in skeletal muscle extend to satellite cells in autosomal dominant Emery-Dreifuss muscular dystrophy/limb-girdle muscular dystrophy 1B. *Neuromuscular disorders : NMD* **19**, 29-36 (2009).
11. Gupta, P. *et al.* Genetic and ultrastructural studies in dilated cardiomyopathy patients: a large deletion in the lamin A/C gene is associated with cardiomyocyte nuclear envelope disruption. *Basic research in cardiology* **105**, 365-377 (2010).
12. Sylvius, N. *et al.* In vivo and in vitro examination of the functional significances of novel lamin gene mutations in heart failure patients. *Journal of Medical Genetics* **42**, 639-647 (2005).
13. Sullivan, T. *et al.* Loss of A-type lamin expression compromises nuclear envelope integrity leading to muscular dystrophy. *J Cell Biol* **147**, 913-920 (1999).
14. Nikolova, V. *et al.* Defects in nuclear structure and function promote dilated cardiomyopathy in lamin A/C-deficient mice. *The Journal of clinical investigation* **113**, 357-369 (2004).
15. Uchino, R., Nonaka, Y.K., Horigome, T., Sugiyama, S. & Furukawa, K. Loss of Drosophila A-type lamin C initially causes tendon abnormality including disintegration of cytoskeleton and nuclear lamina in muscular defects. *Dev Biol* **373**, 216-227 (2013).
16. Dialynas, G. *et al.* LMNA variants cause cytoplasmic distribution of nuclear pore proteins in Drosophila and human muscle. *Hum Mol Genet* **21**, 1544-1556 (2012).
17. Mounkes, L.C., Kozlov, S.V., Rottman, J.N. & Stewart, C.L. Expression of an LMNA-N195K variant of A-type lamins results in cardiac conduction defects and death in mice. *Human Molecular Genetics* **14**, 2167-2180 (2005).

18. Arimura, T. *et al.* Mouse model carrying H222P-Lmna mutation develops muscular dystrophy and dilated cardiomyopathy similar to human striated muscle laminopathies. *Human molecular genetics* **14**, 155-169 (2004).
19. Pimentel, M.R., Falcone, S., Cadot, B. & Gomes, E.R. In Vitro Differentiation of Mature Myofibers for Live Imaging. *Journal of visualized experiments : JoVE* (2017).
20. Melcon, G. *et al.* Loss of emerin at the nuclear envelope disrupts the Rb1/E2F and MyoD pathways during muscle regeneration. *Human Molecular Genetics* **15**, 637-651 (2006).
21. Bertrand, A.T. *et al.* Cellular microenvironments reveal defective mechanosensing responses and elevated YAP signaling in LMNA-mutated muscle precursors. *Journal of Cell Science* **127**, 2873-2884 (2014).
22. Cohen, T.V. *et al.* Defective skeletal muscle growth in lamin A/C-deficient mice is rescued by loss of Lap2α. *Human molecular genetics* (2013).
23. Zwerger, M. *et al.* Myopathic lamin mutations impair nuclear stability in cells and tissue and disrupt nucleo-cytoskeletal coupling. *Human Molecular Genetics* **22**, 2335-2349 (2013).
24. Dahl, K.N., Engler, A.J., Pajerowski, J.D. & Discher, D.E. Power-law rheology of isolated nuclei with deformation mapping of nuclear substructures. *Biophysical journal* **89**, 2855-2864 (2005).
25. Discher, D.E., Boal, D.H. & Boey, S.K. Simulations of the erythrocyte cytoskeleton at large deformation. II. Micropipette aspiration. *Biophysical Journal* **75**, 1584-1597 (1998).
26. Fedorchak, G. & Lammerding, J. Cell Microharpooning to Study Nucleo-Cytoskeletal Coupling. *The Nuclear Envelope: Methods and Protocols*, 241-254 (2016).
27. Lombardi, M.L., Zwerger, M. & Lammerding, J. Biophysical assays to probe the mechanical properties of the interphase cell nucleus: substrate strain application and microneedle manipulation. *Journal of visualized experiments : JoVE* (2011).
28. Tan, D. *et al.* Phenotype-Genotype Analysis of Chinese Patients with Early-Onset LMNA-Related Muscular Dystrophy. *PLoS One* **10**, e0129699 (2015).
29. Denais, C.M. *et al.* Nuclear envelope rupture and repair during cancer cell migration. *Science* **352**, 353-358 (2016).
30. Maciejowski, J., Li, Y., Bosco, N., Campbell, P.J. & de Lange, T. Chromothripsis and kataegis induced by telomere crisis. *Cell* **163**, 1641-1654 (2015).
31. Raab, M. *et al.* ESCRT III repairs nuclear envelope ruptures during cell migration to limit DNA damage and cell death. *Science* **352**, 359-362 (2016).
32. Robijns, J. *et al.* In silico synchronization reveals regulators of nuclear ruptures in lamin A/C deficient model cells. *Scientific reports* **6**, 30325 (2016).
33. De Vos, W.H. *et al.* Repetitive disruptions of the nuclear envelope invoke temporary loss of cellular compartmentalization in laminopathies. *Hum Mol Genet* **20**, 4175-4186 (2011).
34. Hatch, E.M. & Hetzer, M.W. Nuclear envelope rupture is induced by actin-based nucleus confinement. *J Cell Biol* **215**, 27-36 (2016).
35. Vargas, J.D., Hatch, E.M., Anderson, D.J. & Hetzer, M.W. Transient nuclear envelope rupturing during interphase in human cancer cells. *Nucleus* **3**, 88-100 (2012).
36. Park, S.-J. *et al.* DNA-PK promotes the mitochondrial, metabolic, and physical decline that occurs during aging. *Cell metabolism* **25**, 1135-1146. e1137 (2017).

37. Gimpel, P. *et al.* Nesprin-1α-dependent microtubule nucleation from the nuclear envelope via Akap450 is necessary for nuclear positioning in muscle cells. *Current Biology* **27**, 2999 (2017).
38. Irianto, J. *et al.* Nuclear constriction segregates mobile nuclear proteins away from chromatin. *Molecular biology of the cell* **27**, 4011-4020 (2016).
39. Blackford, A.N. & Jackson, S.P. ATM, ATR, and DNA-PK: The Trinity at the Heart of the DNA Damage Response. *Molecular Cell* **66**, 801-817 (2017).
40. Larsen, B.D. *et al.* Caspase 3/caspase-activated DNase promote cell differentiation by inducing DNA strand breaks. *Proceedings of the National Academy of Sciences* **107**, 4230-4235 (2010).
41. Connolly, P.F. & Fearnhead, H.O. DNA-PK activity is associated with caspase-dependent myogenic differentiation. *The FEBS journal* **283**, 3626-3636 (2016).
42. Wilson, M.H. & Holzbaur, E.L. Nesprins anchor kinesin-1 motors to the nucleus to drive nuclear distribution in muscle cells. *Development* **142**, 218-228 (2015).
43. Roman, W. & Gomes, E.R. Nuclear positioning in skeletal muscle. *Seminars in cell & developmental biology* (2017).
44. Gache, V., Gomes, E.R. & Cadot, B. Microtubule motors involved in nuclear movement during skeletal muscle differentiation. *Mol Biol Cell* **28**, 865-874 (2017).
45. Blackford, A.N. & Jackson, S.P. ATM, ATR, and DNA-PK: The Trinity at the Heart of the DNA Damage Response. *Mol Cell* **66**, 801-817 (2017).
46. Gonzalo, S. DNA damage and lamins. *Adv Exp Med Biol* **773**, 377-399 (2014).
47. Hatch, E.M. Nuclear envelope rupture: little holes, big openings. *Curr Opin Cell Biol* **52**, 66-72 (2018).
48. Shah, P., Wolf, K. & Lammerding, J. Bursting the Bubble - Nuclear Envelope Rupture as a Path to Genomic Instability? *Trends Cell Biol* **27**, 546-555 (2017).
49. Schwartz, L.M. Atrophy and programmed cell death of skeletal muscle. *Cell death and differentiation* **15**, 1163-1169 (2008).
50. Chung, J.H. The role of DNA-PK in aging and energy metabolism. *FEBS J* **285**, 1959-1972 (2018).
51. Kotula, E. *et al.* DNA-PK target identification reveals novel links between DNA repair signaling and cytoskeletal regulation. *PLoS One* **8**, e80313 (2013).
52. Wallace, G.Q. & McNally, E.M. Mechanisms of muscle degeneration, regeneration, and repair in the muscular dystrophies. *Annual review of physiology* **71**, 37-57 (2009).
53. Mejat, A. *et al.* Lamin A/C-mediated neuromuscular junction defects in Emery-Dreifuss muscular dystrophy. *J Cell Biol* **184**, 31-44 (2009).
54. Gnocchi, V.F. *et al.* Uncoordinated transcription and compromised muscle function in the lmna-null mouse model of Emery-Dreyfuss muscular dystrophy. *PLoS One* **6**, e16651 (2011).
55. Puckelwartz, M. Emery–Dreifuss muscular dystrophy, in *Handbook of clinical neurology*, Vol. 101 155-166 (Elsevier, 2011).
56. Bogdanovich, S., Gardner, B. & McNally, E. Abnormal Muscle Pathology and Physiology, in *Cardioskeletal Myopathies in Children and Young Adults* 65-82 (Elsevier, 2017).
57. Thijssen, R. *et al.* Dual TORK/DNA-PK inhibition blocks critical signaling pathways in chronic lymphocytic leukemia. *Blood* **128**, 574-583 (2016).

58. McGregor, A.L., Hsia, C.R. & Lammerding, J. Squish and squeeze-the nucleus as a physical barrier during migration in confined environments. *Curr Opin Cell Biol* **40**, 32-40 (2016).
59. Gundersen, G.G. & Worman, H.J. Nuclear positioning. *Cell* **152**, 1376-1389 (2013).
60. Wu, Y.K., Umeshima, H., Kurisu, J. & Kengaku, M. Nesprins and opposing microtubule motors generate a point force that drives directional nuclear motion in migrating neurons. *Development* **145** (2018).
61. Jung, H.J. *et al.* Regulation of prelamin A but not lamin C by miR-9, a brain-specific microRNA. *Proc Natl Acad Sci U S A* **109**, E423-431 (2012).
62. Coffinier, C. *et al.* Deficiencies in lamin B1 and lamin B2 cause neurodevelopmental defects and distinct nuclear shape abnormalities in neurons. *Mol Biol Cell* **22**, 4683-4693 (2011).
63. Bulfield, G., Siller, W.G., Wight, P.A. & Moore, K.J. X chromosome-linked muscular dystrophy (mdx) in the mouse. *Proc Natl Acad Sci U S A* **81**, 1189-1192 (1984).
64. Springer, M.L., Rando, T.A. & Blau, H.M. Gene delivery to muscle. *Current protocols in human genetics / editorial board, Jonathan L. Haines ... [et al.]* **Chapter 13**, Unit13.14-Unit13.14 (2002).
65. Civril, F. *et al.* Structural mechanism of cytosolic DNA sensing by cGAS. *Nature* **498**, 332-337 (2013).
66. Vogler, T.O., Gadek, K.E., Cadwallader, A.B., Elston, T.L. & Olwin, B.B. Isolation, Culture, Functional Assays, and Immunofluorescence of Myofiber-Associated Satellite Cells. *Methods in molecular biology* **1460**, 141-162 (2016).
67. Arimura, T. *et al.* Nuclear accumulation of androgen receptor in gender difference of dilated cardiomyopathy due to lamin A/C mutations. *Cardiovasc Res* **99**, 382-394 (2013).

FIGURES

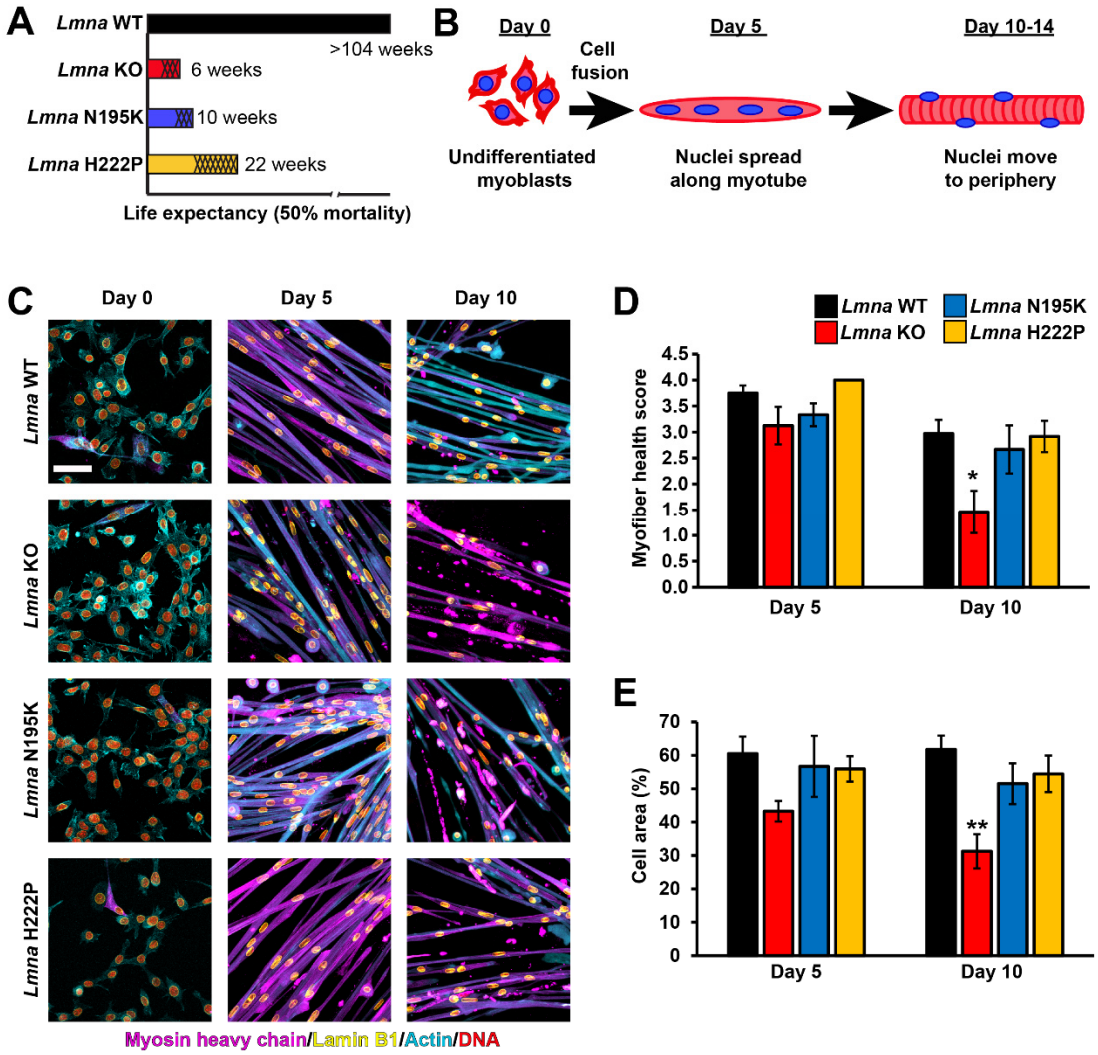

Figure 1. *In vitro* differentiated primary myoblasts from *Lmna* KO, *Lmna* N195K, and *Lmna* H222P mice recapitulates disease severity. (**A**) Graphical representation of the three *Lmna* mutant models used in the study, indicating the published 50% mortality rates of *Lmna* KO, *Lmna* N195K, and *Lmna* H222P mice, as well as wild-type (*Lmna* WT) controls. Shading represents the onset of disease symptoms in the mouse models. (**B**) Schematic for the stages of differentiation from primary myoblasts into mature myofibers in the *in vitro* system. (**C**) Representative images of *Lmna* WT, *Lmna* KO, *Lmna* N195K and *Lmna* H222P primary skeletal muscle cells at days 0, 5 and 10 of differentiation. Scale bar = 100 µm. (**D**) Quantification of myofiber health at days 5 and 10 of differentiation. Fibers were assigned health scores from 0 (worst) to 4 (best) based on their visual appearance, as defined in Suppl. Fig. S3. n = 3-5 independent cell lines for each genotype. *, $p < 0.05$ vs. *Lmna* WT. (**D**) Quantification of cellular area using myosin heavy chain and F-actin fluorescence at days 5, 10 of differentiation. n = 3-6 independent cell lines for each genotype. **, $p < 0.01$ vs. *Lmna* WT.

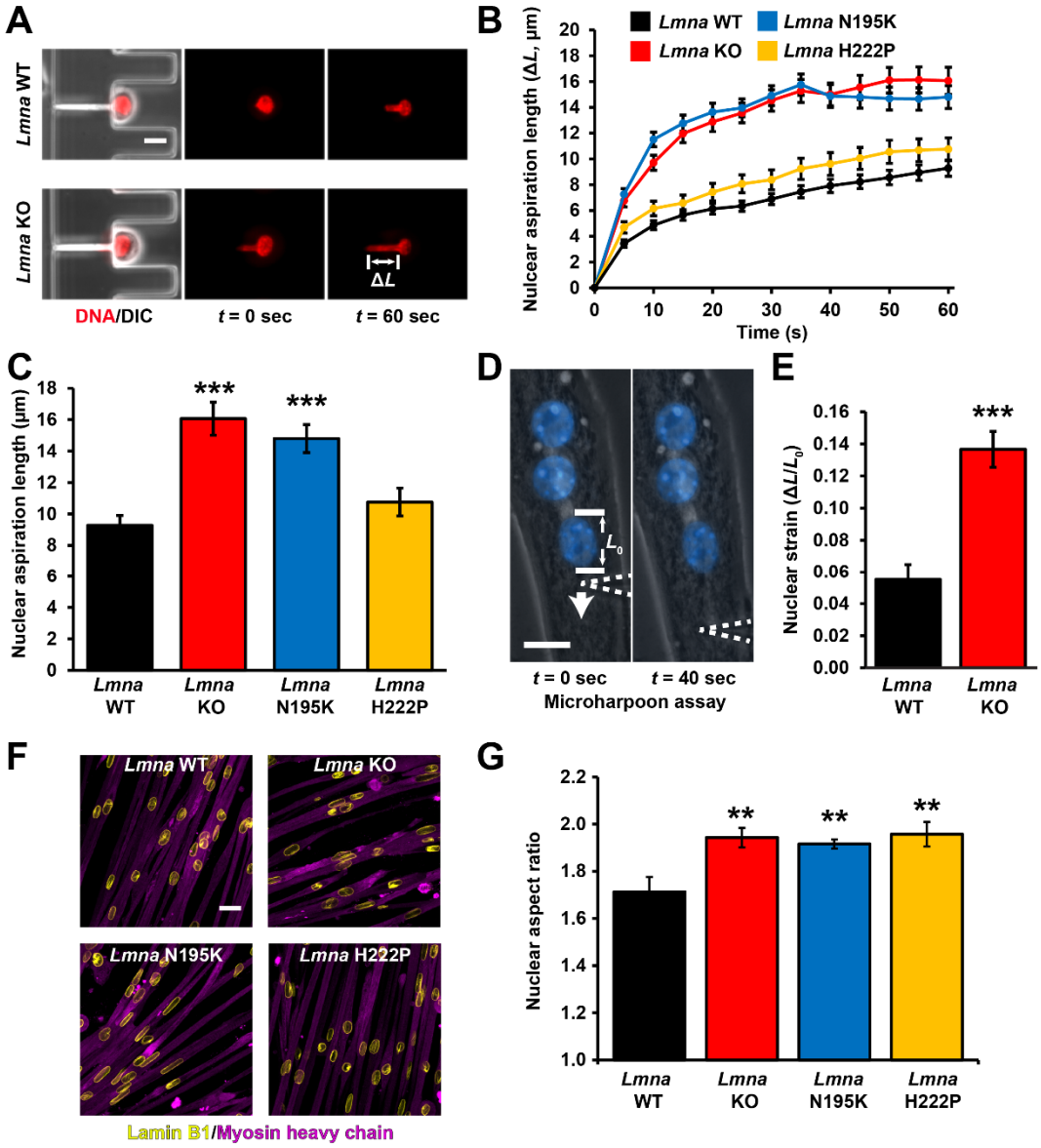

Figure 2. *Lmna* mutant muscle cells display defects in nuclear stability. (**A**) Representative images of *Lmna* WT and *Lmna* KO nuclei deforming in a microfluidic micropipette aspiration device. Scale bar = 10 µm. (**B**) Measurement for nuclear deformation at 5 second intervals for *Lmna* WT, *Lmna* KO, *Lmna* N195K, and *Lmna* H222P myoblasts during 60 seconds of aspiration. (**C**) Quantification of the nuclear deformation after 60 seconds of aspiration. n = 41-67 nuclei per genotype from 3 independent experiments. ***, $p < 0.001$ *vs*. *Lmna* WT. (**D**) Microharpoon assay to measure nuclear deformability ($\Delta L/L_0$) in myofibers, showing representative images before and at the end of perinuclear cytoskeletal strain application with a microneedle (dashed line). Scale bar = 15 µm. (**E**) Quantification of nuclear strain induced by microharpoon assay in *Lmna* WT and *Lmna* KO myotubes at day 5 of differentiation. n = 19-22 nuclei per genotype from 3 independent experiments. ***, $p < 0.001$ *vs*. *Lmna* WT myotubes. (**F**) Representative image of nuclear morphology in *Lmna* WT, *Lmna* KO, *Lmna* N195K and *Lmna* H222P myotubes after 5 days of differentiation. Scale bar = 20 µm (**G**) Nuclear aspect ratio (length/width) in *Lmna* WT, *Lmna* KO, *Lmna* N195K and *Lmna* H222P myotubes after 5 days of differentiation. n = 3 - 4 independent cell lines per genotype with >100 nuclei counted per image. *, $p < 0.05$ *vs*. *Lmna* WT.

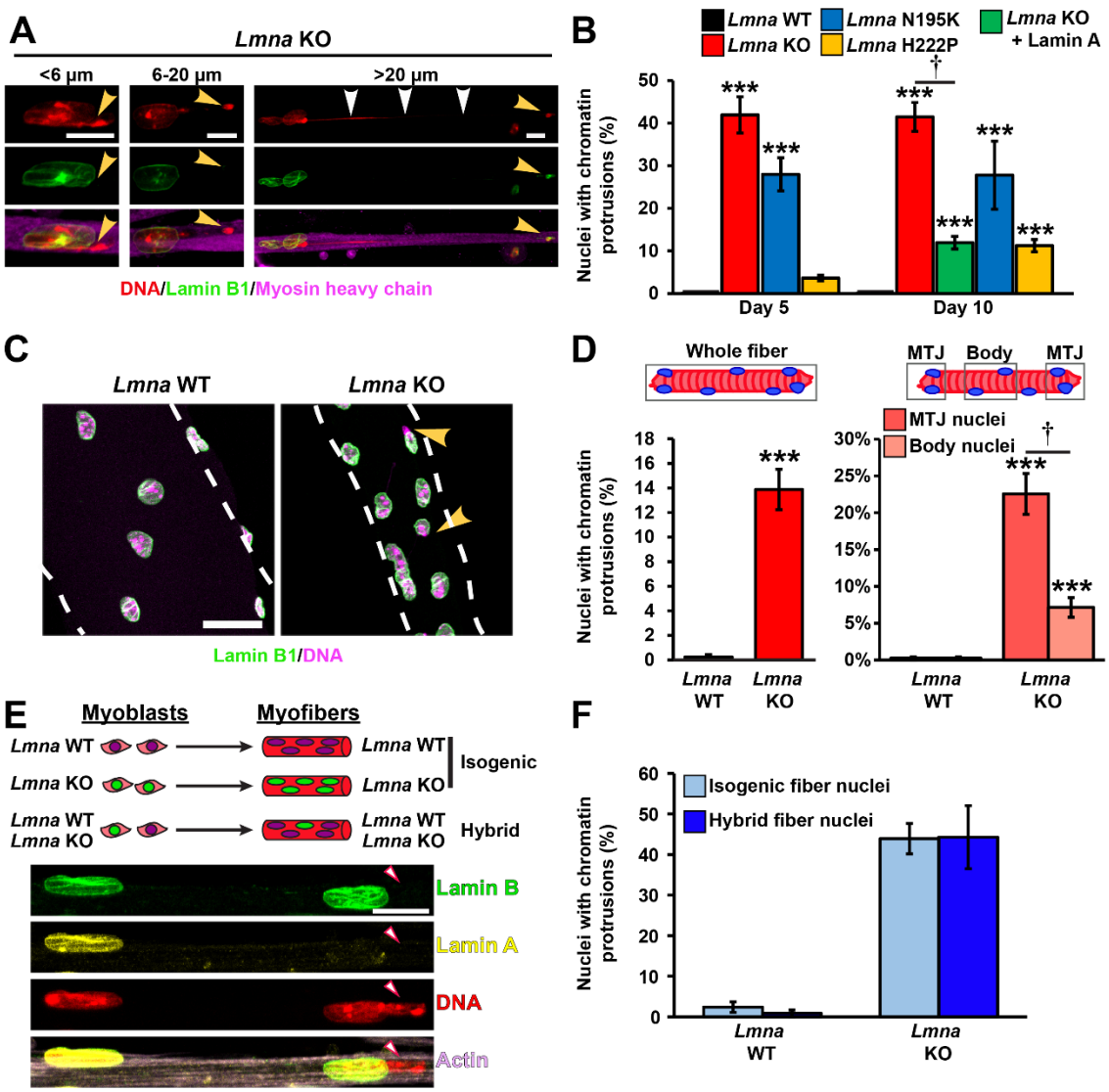

Figure 3. *Lmna* mutant myonuclei develop chromatin protrusions during differentiation. (**A**) Representative images of chromatin protrusions observed in *Lmna* KO myofibers after 10 days of differentiation. Yellow arrowheads indict the end of the protrusion; the white arrowheads indicate a thin chromatin tether protruding from the nucleus. Scale bar = 10 µm. (**B**) Quantification of the percentage of myonuclei containing chromatin protrusion at days 5 and 10 of differentiation in *Lmna* WT, *Lmna* KO, *Lmna* KO + Lamin A, *Lmna* N195K and *Lmna* H222P cell lines. Data from $n = 3$ independent experiments with 62-73 nuclei per genotype. ***, $p < 0.001$ *vs*. *Lmna* WT cells. †, $p < 0.01$ *vs*. *Lmna* KO. (**C**) Representative images of isolated single muscle fibers from *Lmna* WT and *Lmna* KO mice labeled for lamin B1 (green) and DNA (magenta). Arrowheads indicate the presence of chromatin protrusions in *Lmna* KO muscle fiber. Scale bar = 20 µm. (**D**) Quantification of the percentage of myonuclei with chromatin protrusion in isolated muscle fibers from *Lmna* WT and *Lmna* KO mice. Left, data based on analysis of total muscle fiber. Right, analysis for nuclei located at the MTJ compared to those within the body of the fiber. n = 8-11 mice per genotype, with 5 single fibers imaged per animal. ***, $p < 0.001$ *vs*. *Lmna* WT. †, $p < 0.01$ *vs*. nuclei in the muscle body. (**E**) Top, schematic of the generation of hybrid myofibers containing nuclei from both *Lmna* WT and *Lmna* KO cell lines. Bottom, corresponding representative images. Final hybrid fibers contained ~80% *Lmna* WT nuclei and 20% *Lmna* KO nuclei. Arrowheads denote *Lmna* KO nucleus with a chromatin protrusion residing within the same myofiber as a *Lmna* WT nucleus. (**F**)

Quantification of the number of chromatin protrusions from *Lmna* WT and *Lmna* KO contained within isogenic myofibers (control) or hybrid myofibers containing 80% *Lmna* WT and 20% *Lmna* KO nuclei. *n* = 3 independent experiments, in which 91-163 nuclei were quantified per experiment.

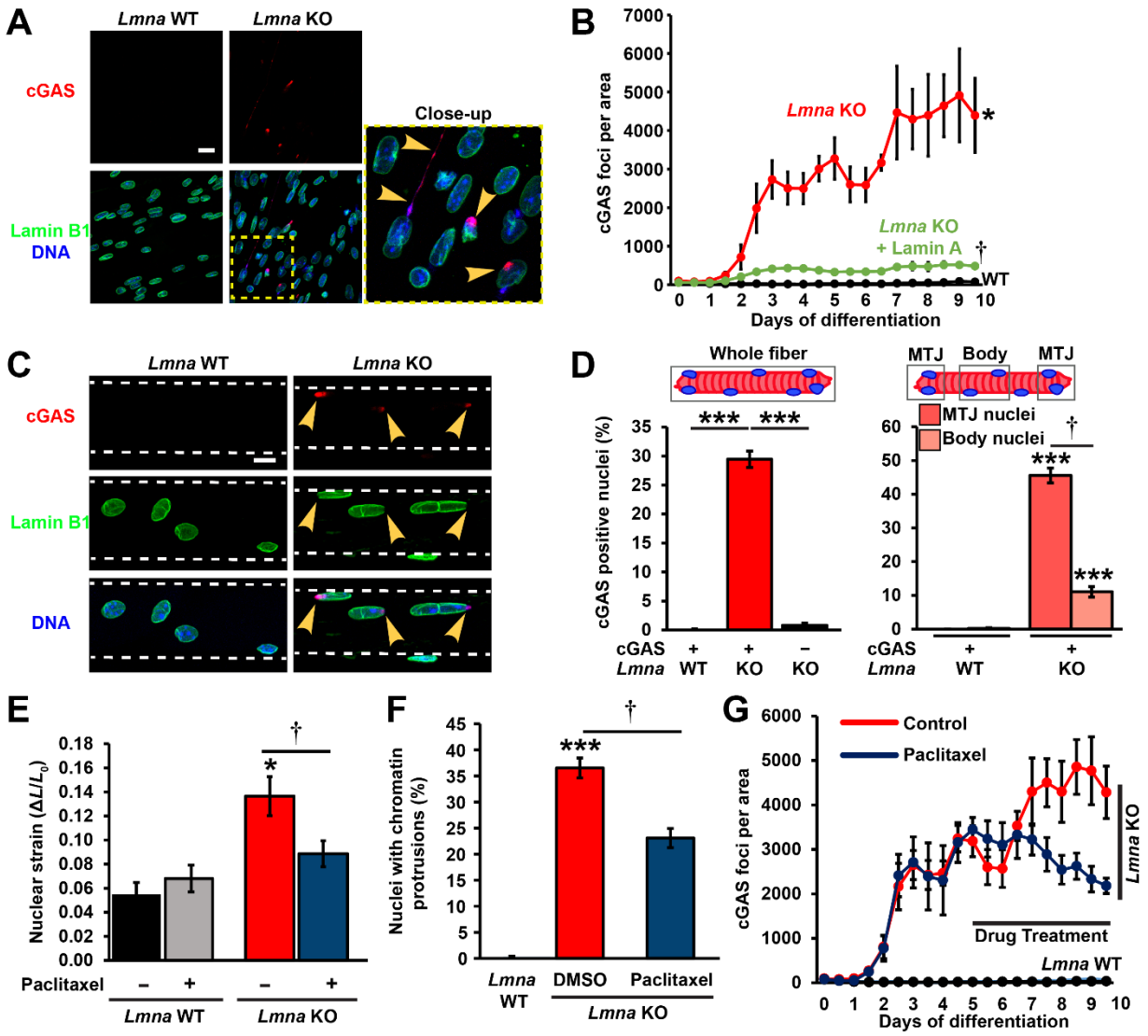

Figure 4. *Lmna* mutant myonuclei undergo nuclear envelope rupture *in vitro* and *in vivo*. (**A**) Representative images of the accumulation of cGAS-mCherry at the sites of nuclear envelope rupture in *Lmna* KO myonuclei at day 5 of differentiation. Scale bar = 20µm. (**B**) Quantification of cGAS-mCherry foci formation per field of view during myofiber differentiation in *Lmna* WT, *Lmna* KO, and *Lmna* KO cells expressing ectopic lamin A, expressed. $n = 3$ independent experiments. *, $p < 0.05$ vs. *Lmna* WT. †, $p < 0.01$ vs. *Lmna* KO. (**C**) Representative maximum intensity projection images of single muscle fibers from *Lmna* WT and *Lmna* KO mice expressing a cGAS-tdTomato nuclear envelope rupture reporter, showing accumulation of cGAS-tdTomato at the site of nuclear envelope rupture in *Lmna* KO muscle fibers. Scale bar = 10 µm. (**D**) Quantification of the percentage of myonuclei positive for cGAS-tdTomato foci in isolated muscle fibers from *Lmna* WT and *Lmna* KO mice expressing the cGAS-tdTomato transgene (cGAS+) or non-expressing littermates (cGAS–). Analysis performed for whole fiber (left) and by classification of nuclei located at the MTJ or within the body of the fiber (right). n = 5-8 mice per genotype, with 5 fibers per animal. ***, $p < 0.001$ *vs*. *Lmna* WT. †, $p < 0.01$ *vs*. nuclei in the muscle body. (**E**) Quantification of nuclear strain in *Lmna* WT and *Lmna* KO myofibers using microharpoon assay following 24 hours of treatment with 50 nM paclitaxel or DMSO vehicle control. *, $p < 0.05$ *vs*. *Lmna* WT. †, $p < 0.05$ *vs*. vehicle control. (**F**) Quantification of chromatin protrusions at day 7 of differentiation following treatment with the paclitaxel (50 nM) or DMSO starting at day 4. $n = 3$ independent experiments. ***, $p < 0.001$ *vs*. *Lmna*

WT. †, $p < 0.01$ *vs*. vehicle control. (**G**) Quantification of cGAS-mCherry foci formation during 10 myofiber differentiation following treatment with paclitaxel (10 nM) or DMSO control, starting at day 5 of differentiation. $n = 3$ independent experiments.

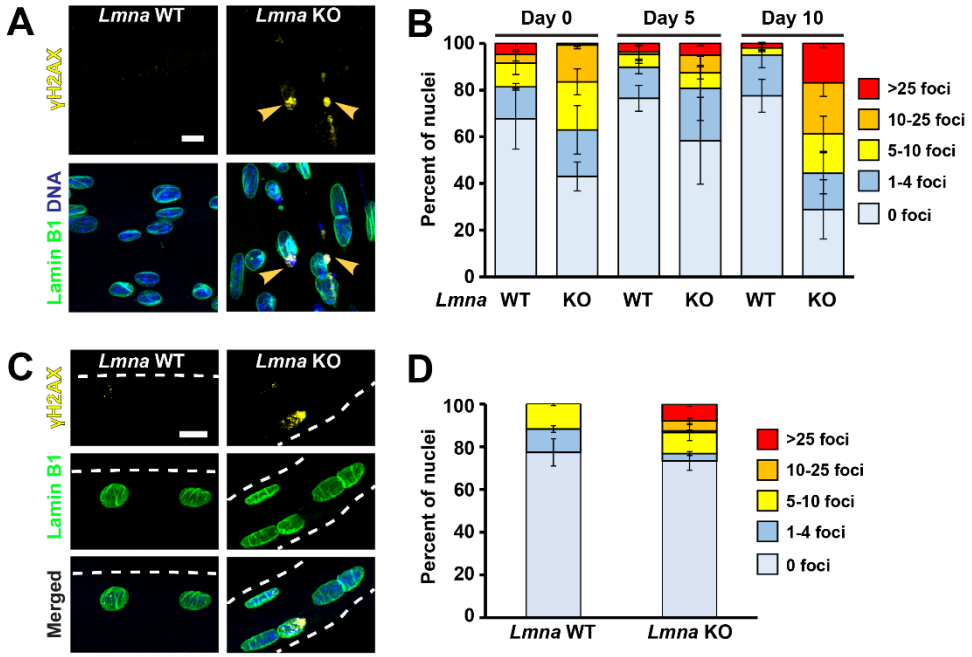

Figure 5. *Lmna* KO mice have increased DNA damage in myonuclei *in vitro* and *in vivo*. (**A**) Representative images of γH2AX foci, a marker of a double-stranded DNA break, in *Lmna* KO myonuclei. Arrowheads indicated γH2AX foci at the sites of chromatin protrusions. Scale bar = 10 µm. (**B**) Quantification of the extent of DNA damage based on the number of γH2AX foci per nucleus during myofiber differentiation. *Lmna* KO myonuclei show a progressive increase in the amount of severe DNA damage during myofiber differentiation. n = 3 independent cell lines per genotype. (**C**) Representative images of γH2AX foci in isolated single muscle fibers from *Lmna* WT and *Lmna* KO mice. Scale bar = 10 µm. (**D**) Quantification of the extent of DNA damage based on the number of γH2AX foci per nucleus in isolated single fibers. n = 3-5 mice per genotype in which 5 fibers are imaged per animal.

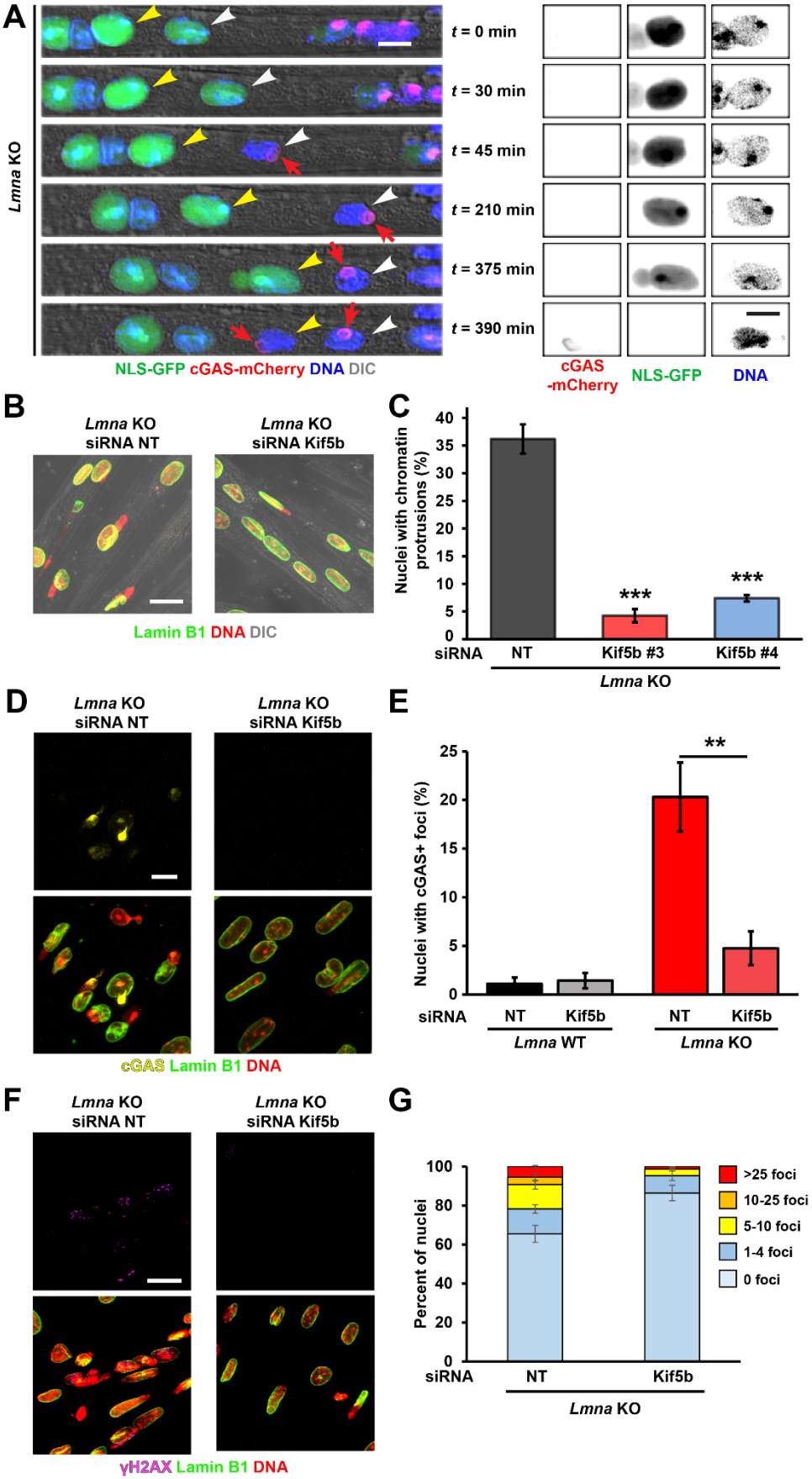
A
Lmna KO
t = 0 min
t = 30 min
t = 45 min
t = 210 min
t = 375 min
t = 390 min
NLS-GFP cGAS-mCherry DNA DIC
cGAS -mCherry
NLS-GFP
DNA
B
Lmna KO siRNA NT
Lmna KO siRNA Kif5b
Lamin B1 DNA DIC
C
Nuclei with chromatin protrusions (%)
40
35
30
25
20
15
10
5
0
***
***
siRNA
NT
Kif5b #3
Kif5b #4
Lmna KO
D
Lmna KO siRNA NT
Lmna KO siRNA Kif5b
cGAS Lamin B1 DNA
E
Nuclei with cGAS+ foci (%)
25
20
15
10
5
0
**
siRNA
NT
Kif5b
NT
Kif5b
Lmna WT
Lmna KO
F
Lmna KO siRNA NT
Lmna KO siRNA Kif5b
γH2AX Lamin B1 DNA
G
Percent of nuclei
100
80
60
40
20
0
>25 foci
10-25 foci
5-10 foci
1-4 foci
0 foci
siRNA
NT
Kif5b
Lmna KO

Figure 6. Myonuclear ruptures occur during nuclear migration in *Lmna* KO myotubes. (**A**) Representative time-lapse image sequence of nuclear envelope rupture in *Lmna* KO myonuclei during nuclear migration at day five of differentiation. White and yellow arrowheads mark two individual nuclei that undergo nuclear envelope rupture, visibly by transient loss of NLS-GFP from the nucleus and stable accumulation of cGAS-mCherry at the site of rupture (red arrow). Images on the right show close-ups of the nucleus marked with a yellow arrowhead. Scale bar = 10µm for all images. (**B**) Representative images of *Lmna* KO myofiber at day 5 of differentiation treated with either a non-target control siRNA (siRNA NT) or siRNA against kinesin-1 (siRNA Kif5b) at day 0. Scale bar = 20 µm. (**C**) Quantification of the number of chromatin protrusions at day 5 of differentiation in *Lmna* KO cells treated with non-target (NT) siRNA or depleted for Kif5b using two independent siRNAs (Kif5b#3 and Kif5b#4). $n = 4$ independent experiments, with 155-270 nuclei counted per image. ***, $p < 0.001$ *vs*. NT control. (**D**) Representative images of cGAS-mCherry accumulation in *Lmna* KO cells treated with either non-target control siRNA (siRNA NT) or siRNA against Kif5b. Scale bar = 20 µm (**E**) Quantification of the number of *Lmna* KO myonuclei positive for cGAS-mCherry foci following treatment with either non-target siRNA (siRNA NT) or siRNA against Kif5b. n = 3 independent experiments, in which a total of 911-1383 nuclei per condition were quantified. **, $p < 0.01$ vs. NT. (**F**) Representative images of *Lmna* KO cells treated with either non-target (NT) siRNA or siRNA against Kif5b and immunofluorescently labeled for γH2AX, showing fewer chromatin protrusions and less DNA damage in the Kif5b depleted cells. Scale bar = 20 µm (**G**) Quantification of the number of γH2AX foci in *Lmna* KO myonuclei following treatment with either non-target siRNA or siRNA against Kif5b. n = 3 independent experiments in which 27-53 nuclei are counted per image.

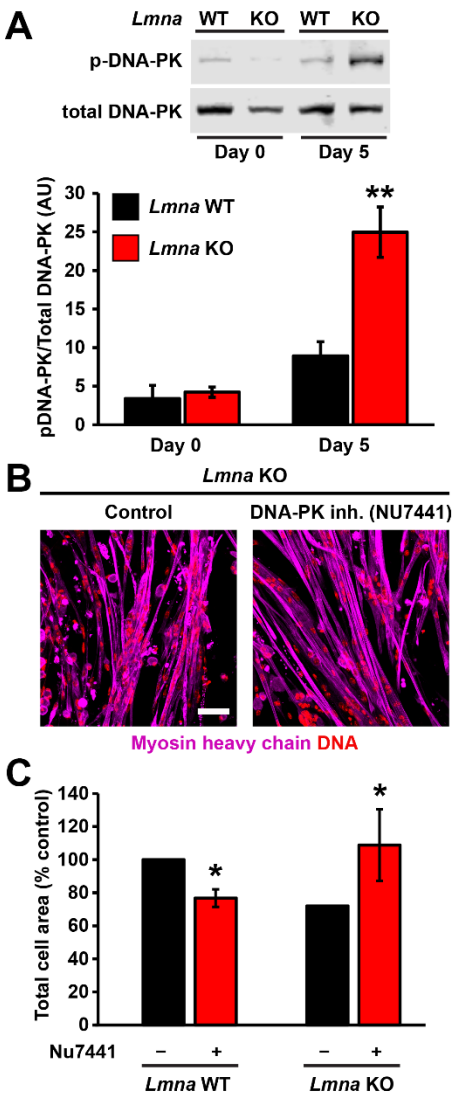

Figure 7. DNA-PK inhibition improves *Lmna* KO myofiber health. (**A**) Quantification of DNA-PK activity in *Lmna* WT and *Lmna* KO myotubes at day 5 of differentiation by probing for the phosphorylation of DNA-PK at S2053, an autophosphorylation specific site. $n = 3$ lysates from independent cell lines. **, $p < 0.01$ *vs*. *Lmna* WT. (**B**) Representative images of *Lmna* KO myofiber health following treatment with the DNA-PK inhibitor NU7441 (1 µM) during days 7-14 of differentiation. Scale bar = 50 µm. (**C**) Quantification of total cell area in *Lmna* WT and *Lmna* KO myofibers following DNA-PK inhibition during days 7-14 of differentiation. n = 3-4 independent cell lines. *, $p < 0.05$ vs. respective genotype DMSO control.

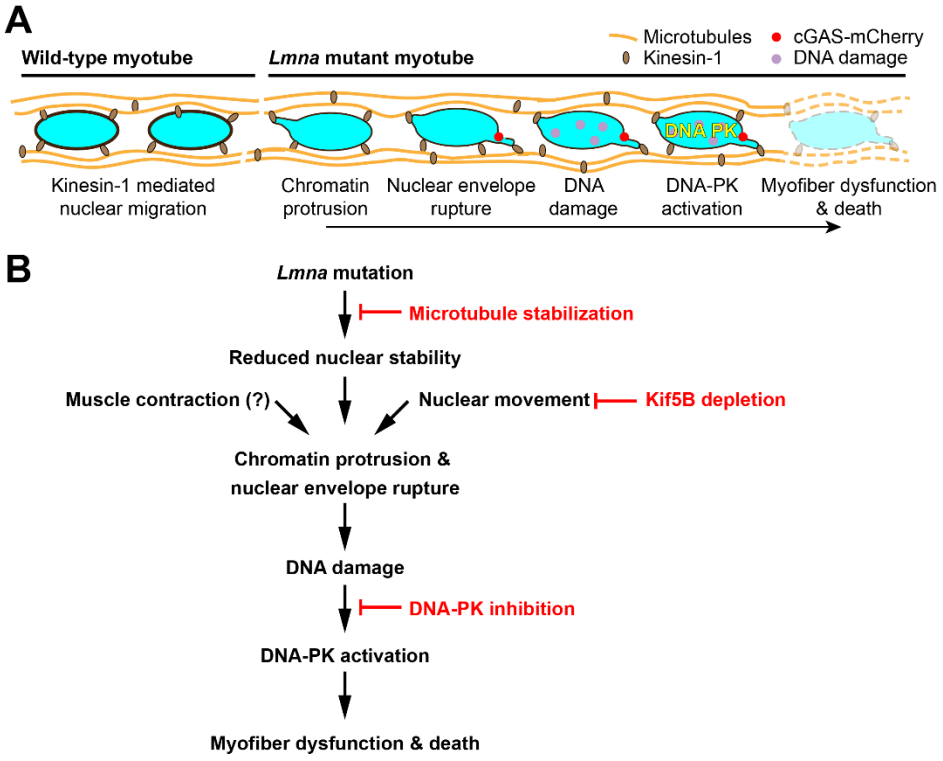

Figure 8. Proposed mechanism by which *Lmna* mutations result in myofiber dysfunction and death. (**A**) Kinesin-1 motor proteins spread myonuclei along the myotubes axis during differentiation. In *Lmna* mutant cells, which have mechanically weaker nuclei, the localized forces associated with nuclear migration cause chromatin protrusion and nuclear envelope ruptures. This mechanically induced nuclear damage results in DNA damage, detected by H2AX foci, and activation of the DNA-PK pathway, which leads to decline in myofiber health and cell death. **(B)** Schematic flow chart delineating the steps described in panel A, along with interventions explored in this work. Stabilizing microtubules surrounding the myonuclei reinforces the *Lmna* mutant nuclei and prevents chromatin protrusions and nuclear envelope ruptures. Inhibiting nuclear movement by Kif5b depletions similarly prevents nuclear damage. Muscle contractions may also contribute to nuclear damage *in vivo*. Inhibiting DNA-PK inhibition rescues myofiber health, despite the continued presence of nuclear damage.